Soft Matter

PAPER

View Article Online
View Journal | View Issue

Cite this: *Soft Matter*, 2016, 12, 5613

Tri-layer wrinkling as a mechanism for anchoring center initiation in the developing cerebellum

Emma Lejeune,[a] Ali Javili,[a] Johannes Weickenmeier,[b] Ellen Kuhl*[b] and Christian Linder*[a]

Received 29th February 2016,
Accepted 23rd May 2016

DOI: 10.1039/c6sm00526h

www.rsc.org/softmatter

During cerebellar development, anchoring centers form at the base of each fissure and remain fixed in place while the rest of the cerebellum grows outward. Cerebellar foliation has been extensively studied; yet, the mechanisms that control anchoring center initiation and position remain insufficiently understood. Here we show that a tri-layer model can predict surface wrinkling as a potential mechanism to explain anchoring center initiation and position. Motivated by the cerebellar microstructure, we model the developing cerebellum as a tri-layer system with an external molecular layer and an internal granular layer of similar stiffness and a significantly softer intermediate Purkinje cell layer. Including a weak intermediate layer proves key to predicting surface morphogenesis, even at low stiffness contrasts between the top and bottom layers. The proposed tri-layer model provides insight into the hierarchical formation of anchoring centers and establishes an essential missing link between gene expression and evolution of shape.

1 Introduction

The cerebellum, the little brain, is a tightly folded structure located at the bottom of the brain. It plays an important role in motor control and higher order functions including cognition, emotion, and language processing.[1] Unlike the cerebrum, the cerebellum is covered with finely spaced parallel grooves that create a morphologically unique appearance, similar to an accordion,[2] see Fig. 1. When completely unfolded, the cerebellar surface covers an area of 5 cm × 1 m. Although it only accounts for 10% of the total brain volume, the cerebellum contains more neurons than the rest of the brain.[3]

The ridges of the cerebellum are called folia, and their formation during cerebellar development is referred to as foliation.[5] Although cerebellar foliation is intensely studied, the mechanisms that direct the initiation and position of individual folia remain insufficiently understood.[1] In the healthy brain, cerebellar foliation follows a tightly regulated sequence of genetically induced events:[2] at the beginning of foliation, anchoring centers form at the base of each fissure. These centers maintain relatively fixed positions as the cerebellar lobes grow outward.[4] The outer cerebellum undergoes a period of rapid anisotropic growth, with faster growth along the anterior–posterior direction, perpendicular to the folia.[6] Altering specific genes changes the onset and location of the anchoring centers and can modulate surface morphogenesis.[7]

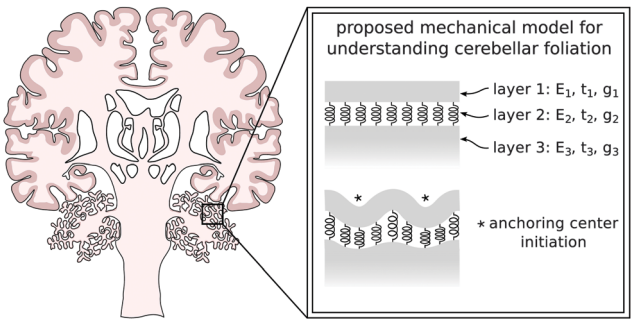

Fig. 1 The cerebellum, the little brain, is a tightly folded structure located at the bottom of the brain. We model cerebellar development using a tri-layer physical model in which anchoring center initiation is a multi-layer wrinkling instability of differential growth between the top and bottom layers.

Understanding the mechanisms of cerebellar foliation is critical because developmental malformations can affect cerebellar structure and, ultimately, cerebellar function including fine movement, equilibrium, posture, and motor learning.[8]

From a physics perspective, the most appealing explanation for cerebellar foliation is the instability phenomenon of growth-induced surface wrinkling.[9–11] Surface wrinkling in the cerebrum has been modeled using a bi-layer model in which compressive stresses from differential growth induce wrinkling instabilities.[12–15] Bi-layer models are widely used to predict surface morphogenesis and pattern formation in engineering structures,[16] geophysics,[17] soft matter physics,[18] and thin films,[19,20] where the upper layer is orders of magnitude stiffer than the lower layer.[21,22] To measure the stiffness in different regions of the brain, we used

[a] Department of Civil and Environmental Engineering, Stanford University, Stanford, CA 94305, USA. E-mail: linder@stanford.edu
[b] Department of Mechanical Engineering, Stanford University, Stanford, CA 94305, USA. E-mail: ekuhl@stanford.edu

Table 1 Regional stiffness variation from nanoindentation

Region	Cerebrum gray matter	Cerebrum white matter	Cerebellum gray & white
Stiffness [kPa]	0.68 ± 0.20	1.41 ± 0.66	0.75 ± 0.29

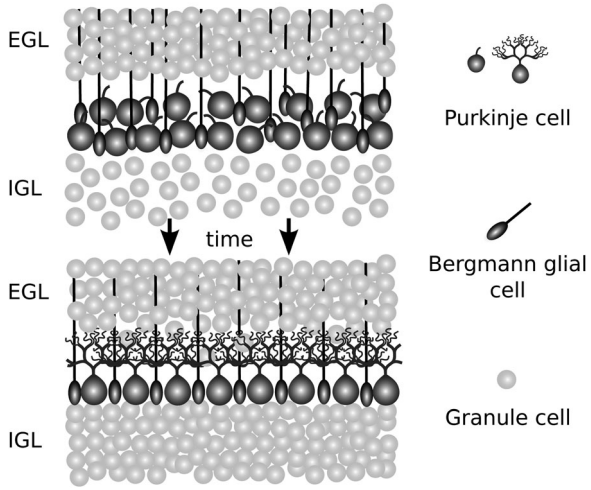

Fig. 2 Evolving layered structure throughout the course of cerebellar development. During development, cells proliferate in the external granular layer (EGL) and migrate to the internal granular layer (IGL).[4] The intermediate Purkinje cell layer changes structure as each cell grows dendrites and the layer transforms from a multi-layer to a mono-layer.[4] At the onset of foliation, the thickness ratio between the EGL and the Purkinje cell layer is much smaller than post-development.

nanoindentation[23] and recorded stiffness values of 0.68 ± 0.20 kPa in the outer gray matter layer and 1.41 ± 0.66 kPa in the inner white matter of the cerebrum, a stiffness contrast of less than one half, see Table 1. The bi-layer folding model, however, fails to predict folding for stiffness contrasts smaller than two.[24,25]

Unlike the cerebrum, the cerebellum consists of three distinct surface layers: an external molecular layer, a thin intermediate Purkinje cell layer, and an internal granular layer, shown in Fig. 2. To illustrate these layers in the developed cerebellum, we stained sagittal slices of a neonatal mammalian cerebellum with luxol fast blue (LFB) and hematoxylin/eosin (H&E), see Fig. 3. In nanoindentation tests, we found that the cerebellar stiffness of 0.75 ± 0.29 kPa was of same order of magnitude as the cerebral stiffness, see Table 1. These observations motivated our hypothesis that a tri-layer model with a soft intermediate Purkinje cell layer can predict the onset of surface wrinkling and cerebellar foliation, even at low stiffness contrasts between the upper and lower layers. The rest of the paper is organized as follows. In Section 3 we describe our proposed physical model of the cerebellum. Then, Section 4 discusses the implications of adopting our model to describe the onset of cerebellar foliation. Concluding remarks are given in Section 5.

2 Model

Here we present our tri-layer model for instability initiation. Previous applications of this tri-layer model involved stiff films

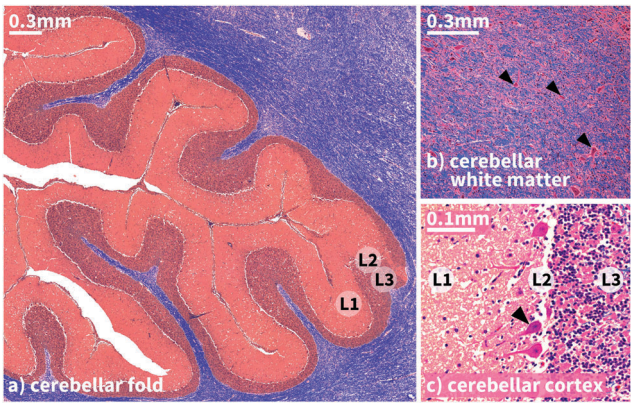

Fig. 3 Sagittal slices of a neonatal mammalian cerebellum stained with luxol fast blue (LFB) and hematoxylin/eosin (H&E) illustrate the three distinct layers of the cerebellum: the external molecular layer (L1), the intermediate Purkinje cell layer (L2), and the internal granular layer (L3). These stains show physical structure post-development, which is significantly different from the structure at the onset of foliation.

adhered to soft substrates, therefore the analytical solution has not been validated in the regime where $E_f \approx E_s$ and the behavior of low-stiffness–contrast tri-layer systems is poorly understood.[26] To address this, we compare the analytical solution to results obtained using the finite element method, described in Section 3.2.

2.1 Analytical model

The essential idea of the tri-layer model is to modify the classical bi-layer film–substrate model[16,17] by reinterpreting the external molecular layer as the film and the combined intermediate layer and internal layer as the substrate.[26] We characterize the tri-layer model through the stiffnesses E_f, E_i, and E_s and thicknesses t_f, t_i and t_s of the film, the intermediate layer, and the substrate. We assume that the cerebellum is incompressible with Poisson's ratios of $\nu_f = \nu_i = \nu_s = 0.5$ and that t_s can be treated as infinite. We begin with the classical Föppl–von Kármán equations[27]

$$\frac{E_f t_f^3}{12}\frac{d^4\omega}{dx^4} + P t_f \frac{d^2\omega}{d\omega} = q \qquad (1)$$

where P is the longitudinal stress in the beam, and film deflection ω and deflection-induced transverse force of the intermediate layer and substrate acting on the film q are functions of the wavenumber n. We adopt a sinusoidal ansatz, $\omega = \omega_0 \cos(nx)$ and define $q = -K\omega_0 \cos(nx)$ where K is the combined intermediate layer and substrate stiffness,[26]

$$K = \frac{2E_s n}{2nt_i(E_s/E_i - 1) + 4}. \qquad (2)$$

The intermediate layer contains Purkinje cells, Bergmann glial cells, and their fibers, see Fig. 4. To account for its pronounced microstructural orientation, we model the intermediate layer as a set of springs.[4,6] With this approach, a tri-layer system with an intermediate layer spring stiffness approaching zero $E_i \to 0$ corresponds to a film, which buckles independently of the substrate with $K \to 0$, while an intermediate layer stiffness

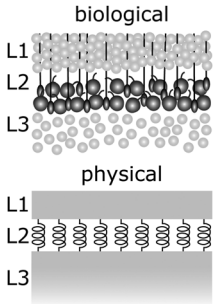

	biological	physical
L1	external molecular layer with rapid growth	film stiffness E_f represents axial and bending strength; fast film growth g_f with $g_f > g_s$
L2	Purkinje cell layer with Bergmann glial cells and aligned, unbraced fibers	intermediate stiffness E_i represents smeared spring stiffness in fiber direction with $E_i < E_f$
L3	internal granular layer with moderate growth	substrate stiffness E_s represents axial and bending strength with combined E_i and E_s smaller than E_f; moderate substrate growth g_s with $g_s < g_f$

Fig. 4 Biological and physical mechanisms of our tri-layer model. Each layer is equipped with its own layer stiffness E, layer thickness t, and growth g. For wrinkling to occur, the external film growth g_f must be greater than the substrate growth g_s and the combined intermediate and substrate stiffnesses E_i and E_s must be less than the film stiffness E_f.

exactly equal to the substrate stiffness $E_i = E_s$ recovers the classical bi-layer model where[26]

$$K = \frac{2E_s}{n}. \tag{3}$$

We insert ω and q into eqn (1) to define the stress in the film P as

$$P = \frac{E_f t_f^2 n^2}{12} + \frac{K}{t_f n^2}. \tag{4}$$

To determine the critical stress P_{cr} and the associated critical wave number n_{cr}, we take the derivative of P with respect to n and set the derivative equal to zero,

$$f(n) = \frac{dP(n)}{dn} = \frac{E_f t_f^3 n^4}{6} + K'n - 2K \doteq 0 \tag{5}$$

with

$$K' = \frac{8E_s}{[2nt_i(E_s/E_i - 1) + 4]^2}. \tag{6}$$

In the bi-layer case, where K is defined with eqn (3), n_{cr} is solved for explicitly,

$$n_{cr} = \sqrt[3]{\frac{3E_s}{E_f}}. \tag{7}$$

For the tri-layer case, we solve the critical condition (5) using an implicit solution scheme and apply Newton's method,

$$f'(n) = \frac{d^2P(n)}{dn^2} = \frac{2E_f t_f^3 n^3}{3} + K''n - K' \tag{8}$$

with

$$K'' = -\frac{32E_s t_i(E_s/E_i - 1)}{[2nt_i(E_s/E_i - 1) + 4]^3} \tag{9}$$

to incrementally update the wave number until the critical condition $f(n)$ drops below a defined tolerance. Once n_{cr} is determined, we calculate the critical stress P_{cr} using eqn (4), and subsequently calculate the critical growth in the film layer and critical wavelength as[26]

$$g_{cr} = \frac{P_{cr}}{E_f - P_{cr}} \quad \text{and} \quad \lambda_{cr} = \frac{2\pi}{n_{cr}}. \tag{10}$$

The outcome of solving these equations is an understanding of when the wrinkling instability will occur through g_{cr}, and an understanding of what the instability mode will look like through λ_{cr}.

2.2 Computational model

A computational model is required to verify the analytical solution in the regime where film and substrate stiffness are approximately equal, $E_f \approx E_s$. We develop a computational model by first treating the entire domain as a continuum where behavior is governed by the balance of linear momentum and instability is driven by the volumetric growth of the film.[32,33] Then, we discretize the domain and solve for g_{cr} and λ_{cr} by performing eigenvalue analysis using the finite element method.[34]

In the continuum setting, we define the deformation gradient $\mathbf{F}$ as $\mathbf{F} = \nabla_{\mathbf{X}}\boldsymbol{\varphi}$ where $\boldsymbol{\varphi}$ is the deformation map, mapping points from the undeformed configuration $\mathbf{X}$ to the deformed configuration $\mathbf{x}$. Then, we multiplicatively decompose the deformation gradient as[35]

$$\mathbf{F} = \mathbf{F}^e\mathbf{F}^g \tag{11}$$

where $\mathbf{F}^e$ is the elastic component of deformation and $\mathbf{F}^g$ is the growth component. As with the analytical solution, we only assume growth in the upper most layer. For consistency with experimental observations,[6] we prescribe growth as transversely isotropic[36] in the direction parallel to the anterior–posterior axis of the cerebellum, which justifies a two dimensional plane–strain model where the medial–lateral axis is captured by the plane-strain condition.

In our continuum model, we treat all materials as isotropic and hyperelastic with a Neo-Hookean free energy of the form

$$\psi = \psi(\mathbf{F}^e) = \frac{1}{2}\mu[\mathbf{F}^e{:}\mathbf{F}^e - 3 - 2\ln J^e] + \frac{1}{2}\lambda\left[\frac{1}{2}\left[(J^e)^2 - 1\right] - \ln J^e\right] \tag{12}$$

where μ and λ are Lamé material parameters, and J^e is the Jacobian $J^e = \det\mathbf{F}^e$, instead of adopting alternative micromechanically motivated material models.[37–39] To capture incompressibility we approximate Poisson's ratio with $\nu = 0.495$. Because unrestrained growth is assumed to be stress free, ψ is expressed as a function of $\mathbf{F}^e$ alone. The first Piola Kirchhoff stress $\mathbf{P}$ follows as

$$\mathbf{P} = \frac{\partial\psi}{\partial\mathbf{F}^e} = \mu\left[\mathbf{F}^e - (\mathbf{F}^e)^{-T}\right] + \frac{1}{2}\lambda\left[(J^e)^2 - 1\right]\mathbf{F}_e^{-T}. \tag{13}$$

Given **P**, quasi-static conditions, and zero body force the balance of linear momentum reduces to

$$\mathrm{Div}\,\mathbf{P} = 0\,. \tag{14}$$

The balance of linear momentum is converted to its weak form, discretized and solved using the finite element framework.[32,34]

For our computational simulations, we take advantage of the fact that the predominant direction of growth is defined by the anterior–posterior axis of the cerebellum and treat the domain as two-dimensional where the medial–lateral axis is captured by the plane strain condition. Given geometric properties (layer thickness) and material properties (layer modulus) we discretize the domain with quadratic elements and run simulations using an in-house nonlinear finite element code. We are able to compute g_{cr} and λ_{cr} by performing eigenvalue analysis on the stiffness matrix of the system. We use the bi-section method to determine the level of growth that causes the stiffness matrix to become singular, g_{cr}, and examine the associated eigenvector to determine λ_{cr}.[34]

Fig. 5 shows representative numerical results where each point plotted (marked with symbols) represents one simulation run. The plots in the upper two rows of Fig. 5, left and center columns, indicate that the analytical and numerical solutions are in excellent agreement. These initial simulations to validate the analytical solution were conducted on a flat domain. Additional simulations were then conducted on a circular (cylindrical) domain, where R defines the distance between the center of the circle and the lower edge of the intermediate layer. The plots in the lower row of Fig. 5 indicate that growth of the outer film in a tri-layer circular domain will follow the same qualitative trends as growth of the upper film in a flat domain. And, notably, as curvature $1/R$ increases, g_{cr} increases as well. This is consistent with the wrinkling behavior of bi-layer systems discussed in the literature.[40,41] In future work, the computational model is required for analysis because the analytical solution uses the small strain assumption, assumes a flat domain, and ignores boundary effects. Furthermore, to quantitatively describe and predict folia formation beyond the onset of the instability, we would have to use an entirely numerical approach.

3 Results and discussion

Fig. 5, upper and middle right, demonstrates that unlike the bi-layer model, the tri-layer model can realistically predict wrinkling at low stiffness contrasts when $E_f \approx E_s$. Fig. 6 illustrates how instability initiation can serve as a mechanism to explain anchoring center initiation. Consistent with experimental observations where multiple anchoring centers form in unison,[4] the coordinated appearance of anchoring centers can be attributed to simultaneously reaching the critical growth value g_{cr}. The associated critical wavelength λ_{cr} dictates the number of anchoring centers. Anchoring centers form at the troughs of the emerging instability pattern. Cells located in the troughs experience compression and an altered physical environment, which could potentially induce further changes in cell behavior and gene expression.[42,43] Our model predicts that the distance between anchoring centers λ_{cr} will be on the order of $5t_f - 15t_f$. This is a good approximation of the distance between anchoring centers at the time of formation in the mouse brain.[4] Across species, the thickness of the cerebellum remains approximately constant[44] while the degree of foliation increases with size, similar to the behavior seen in cortical gyrification,[45] where there is strong evidence that differential growth drives pattern formation.[15] In addition, a differential growth driven instability is consistent with the folia of the cerebellum arising perpendicular to the direction of maximum growth.[6]

Interpreting surface instabilities as the mechanism by which anchoring centers form opens a new path for correlating gene expression to cerebellar foliation. For example, genes that are related to altering the timing of anchoring center formation are immediately connected to changes in the number of anchoring centers and to the cerebellar morphology at the end of development.[4] Studies suggest that this final morphology is highly sensitive to the granular cell proliferation rate,[46] the thickness of the external granular layer, and the number of primary lobules.[47] Our physics-based model for anchoring center initiation makes the connection between timing, through g_{cr}, and shape, through λ_{cr}, straightforward. From eqn (2) and (4) and Fig. 7 it is clear that E_f, E_i, E_s, t_f, and t_i influence timing g_{cr} and shape λ_{cr}. The numerical results shown in Fig. 5 indicate that the degree of curvature influences both g_{cr} and λ_{cr}. In addition, the ratio between film and substrate growth, g_f and g_s, influences instability initiation.[32] For example, genetically altering mice to increase the level of sonic hedgehog (shh) signaling is known to increase granular cell proliferation and subsequently lead to an additional fissure, while altering mice to decrease the level of shh signaling will decrease granular cell proliferation and inhibit fissure formation.[5] Our model connects these changes in granular cell proliferation g_f to g_{cr}, which must be exceeded for fissures to form, providing a link between shh signaling and foliation. Our physical model provides a framework to formalize correlations between altered gene expression on the cellular scale and tissue scale evolution of shape through these parameters.

With regard to the connection between tri-layer wrinkling and the hierarchical anchoring center formation that defines lobules and sublobules, there are two significant additional considerations: first, after anchoring centers form, when the external and intermediate layers buckle out of plane, further outward growth can occur without building up substantial compressive stresses.[9] However, recent studies have shown that cell dispersal at the anchoring centers is blocked,[6] which suggests that anchoring centers act as a growth-constraining boundary conditions that shape the individual lobes, lobules, and sublobules. Second, as the cerebellum develops, the geometric and material properties of each layer change, which will locally alter the critical growth g_{cr} and critical wave length λ_{cr}. Limited cell dispersal across the anchoring centers may produce genetically distinct folia with distinct critical growth g_{cr} and wavelength λ_{cr}.[6]

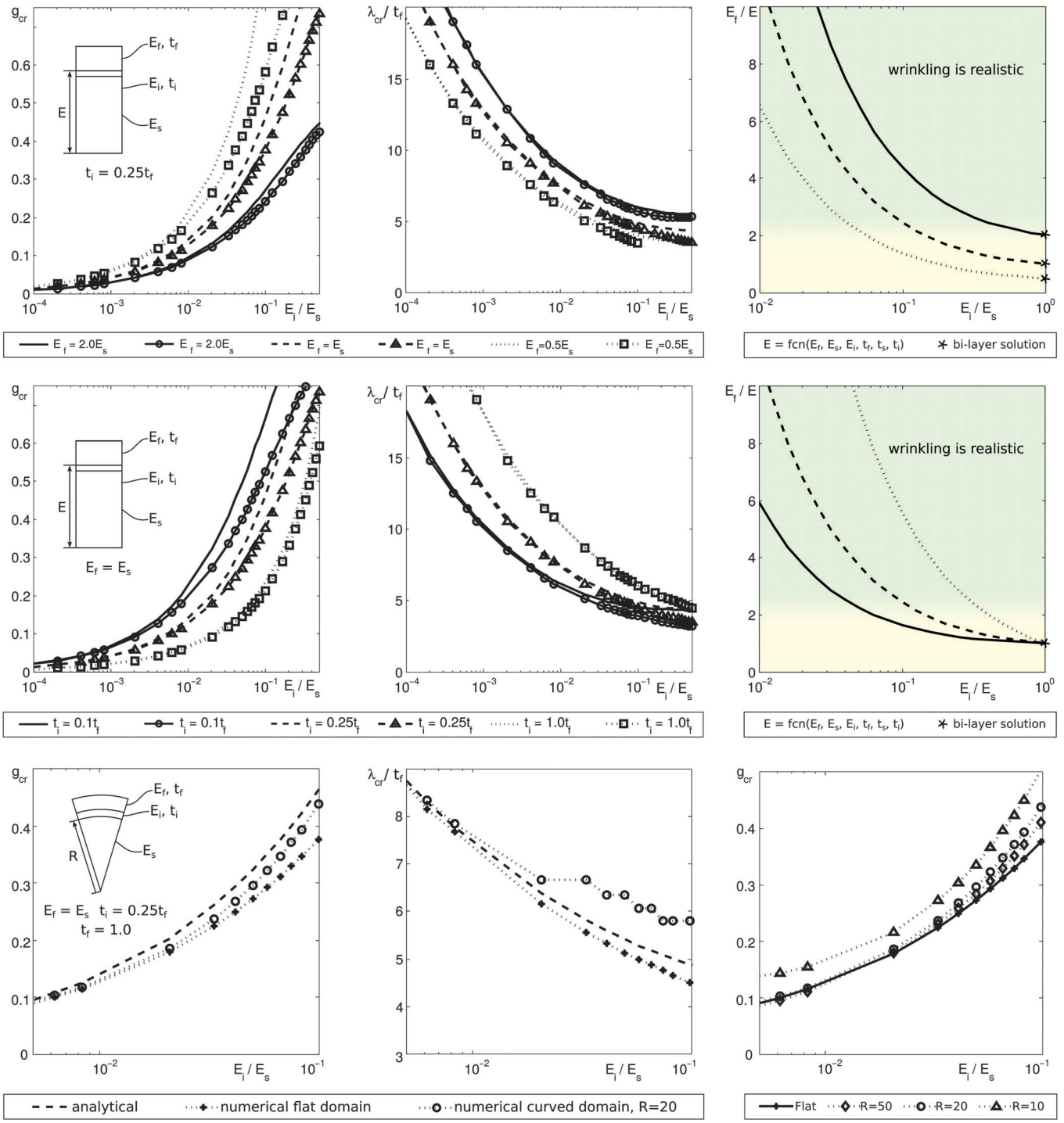

Fig. 5 The upper two rows show critical growth g_{cr}, relative wavelength λ_{cr}/t_f, and relative film to combined intermediate layer and substrate stiffness E_f/E for varying intermediate layer stiffness E_i. Numerical results (symbols) show good agreement with analytical solution, left and center. The upper row of plots demonstrates the sensitivity of g_{cr} and λ_{cr} to the relative film to substrate stiffness E_f/E_s while the lower row demonstrates the sensitivity to layer thickness t_f/t_i. For all cases plotted, t_i is sufficiently low such that our analytical approach remains valid, tri-layer systems with a thicker intermediate layer require additional treatment.[28,29] The plots in the right column show that unlike the classical bi-layer model, the new tri-layer model can predict wrinkling as the likely first mode of instability for low film-to-substrate stiffness contrasts when $E_f \approx E_s$, right. For systems where $E_f \approx E_i \approx E_s$, differential growth combined with surface imperfections will likely cause crease formation prior to wrinkling.[30,31] The lower row contextualizes results of numerical simulations conducted on a circular domain, where R is the distance between the center of the circle and the bottom of the intermediate layer. The left and center plots demonstrate that g_{cr} and λ_{cr} obtained numerically follow the same qualitative trend as the analytical and numerical solutions on a flat domain. The discrete jumps in wavelength, seen in the center plot, occur because the circular domain is constrained to whole number waves. The right plot demonstrates that an increase in curvature $1/R$ causes an increase in g_{cr} across the entire domain of E_i tested.

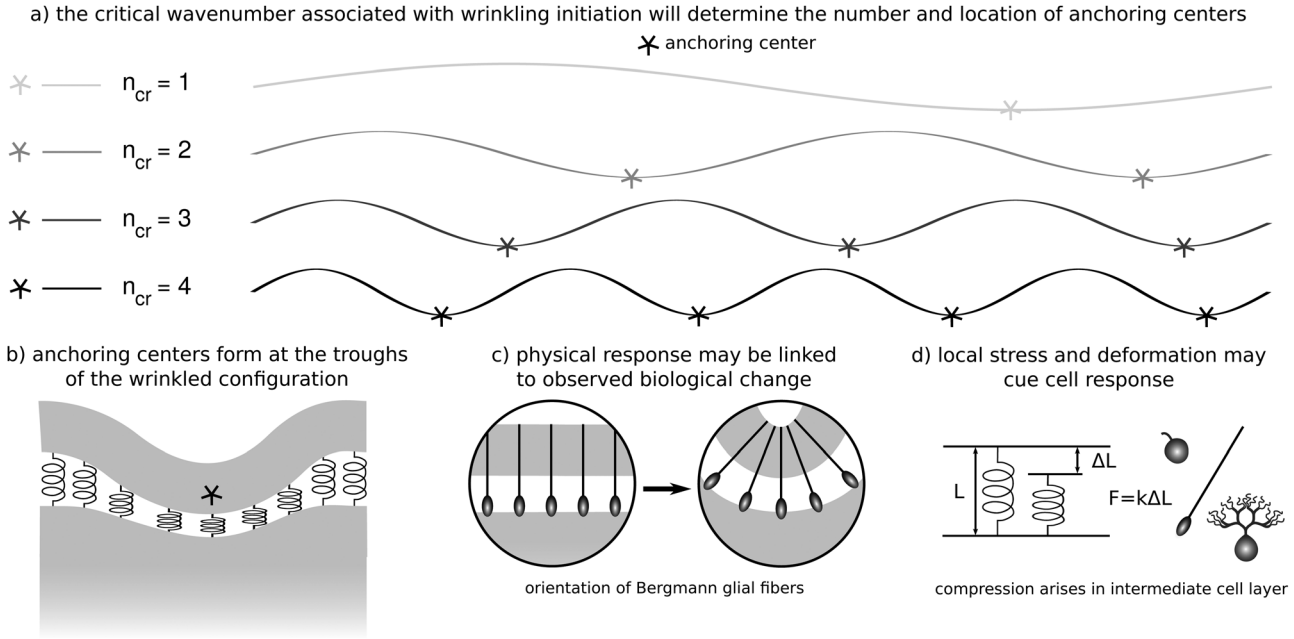

Fig. 6 (a) The wave number $n_{cr} = 2\pi/\lambda_{cr}$, and with it the number of anchoring centers, is sensitive to the layer stiffness as predicted in Fig. 5, center. The folding patterns are the eigenvectors of the wrinkling instability mode. (b) Anchoring centers form at the troughs of the sine waves. (c) Bergmann glial fibers, here represented through springs, fan out from the base of the anchoring center.[4] (d) Cells at the anchoring centers in the intermediate layer experience compression, which may influence cell behavior and induce changes in gene expression that further drive the foliation process.

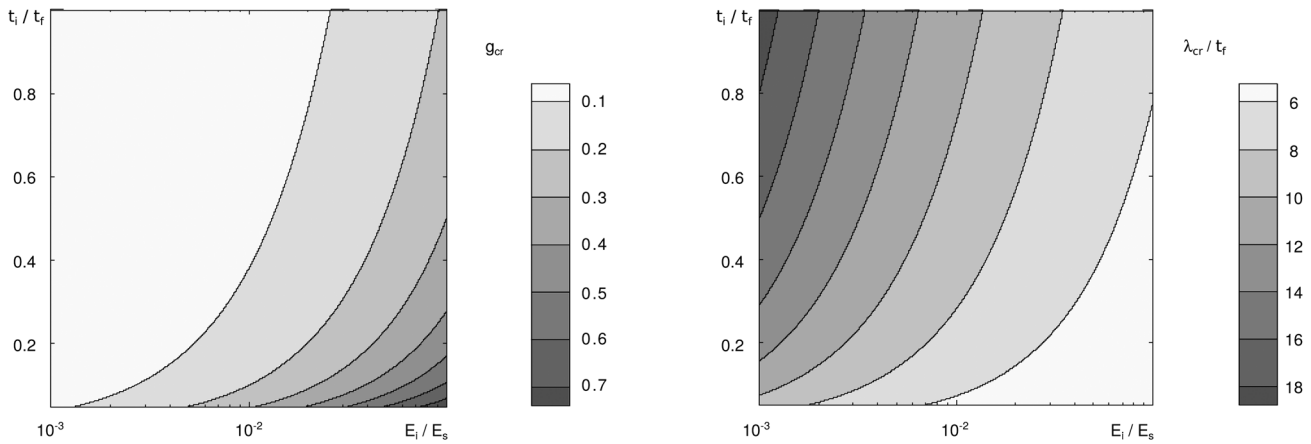

Fig. 7 Timing of anchoring center initiation through g_{cr}, left, and position of anchoring centers through λ_{cr}, right, are altered by changes in material properties E_i/E_s and geometric properties t_i/t_f. Increasing $K_i = E_i/t_i$ increases g_{cr}, left, and decreases λ_{cr}, right. Understanding that geometric instability may be the cause of anchoring center formation establishes a link between parameters which predict g_{cr} and λ_{cr} and the foliation pattern. Both plots correspond to the case where $E_f = E_s$.

This suggests that g_{cr} and λ_{cr} may display significant regional and temporal variations across the developing cerebellum.

Moving forward, the extension of our model for anchoring center initiation to three dimensional irregular domains that more accurately capture the geometry of the cerebellum may provide further insight. A domain which better reflects the shape of the cerebellum will help explain how local variations in curvature, layer thickness, growth rate and material properties regulate the placement of anchoring centers, such that their location is conserved across individuals.[48,49] In addition, the third layer between the film and the substrate may influence the initiation of other types of geometric instability such as creases.[50–52] Finally, the relationship and coupling between biologically driven processes and mechanically driven processes after anchoring center initiation in the post-buckling regime merits further examination. Modeling behavior in this regime is not trivial because the process of fissure formation is characterized by significant changes in the cytoarchitecture at each anchoring center.[4] Based on the information available, it is not obvious how these post-buckling changes impact the mechanical model of the cerebellum. For example, the Bergmann glial fibers schematically illustrated in Fig. 6 fan out from the base of the anchoring

centers and serve as migration trajectories for granular cells.[4] Though the re-orientation of the fibers may be explained by mechanics alone, their influence on cell migration will require additional treatment. And, similar to studies previously conducted in the cerebrum,[53,54] the influence of white matter anisotropy and experimentally observed tension along white matter fibers is worth investigating in the cerebellum.

4 Conclusion

In this paper, we modeled the initiation of the foliation process during cerebellar development using a physics-based tri-layer model. Unlike classical bi-layer models, this new tri-layer model can predict surface wrinkling, even if the stiffnesses of the inner and outer layer are nearly identical. We demonstrated that tri-layer wrinkling is a realistic mechanism for controlling anchoring center initiation and position. We correlated the parameters that control morphogenesis and pattern formation to cellular events and to changes in gene expression. Understanding the mechanisms of cerebellar foliation is critical to interpret developmental malformations associated with movement, equilibrium, posture, and motor learning. This paper provides a new physical perspective to the phenomenon of cerebellar foliation, which has predominantly been studied through a biological lens.

Acknowledgements

Financial support for this research was provided by the National Science Foundation through CAREER Award CMMI-1553638, the National Science Foundation Graduate Research Fellowship under Grant No. DGE-114747, and the Stanford BioX IIP Grant ''Understanding Gyrification Dynamics in the Human Brain''.

References

1 K. Leto, M. Arancillo, E. B. E. Becker, A. Buffo, C. Chiang, B. Ding, W. B. Dobyns, I. Dusart, P. Haldipur, M. E. Hatten, M. Hoshino, A. L. Joyner, M. Kano, D. L. Kilpatrick, N. Koibuchi, S. Marino, S. Martinez, K. J. Millen, T. O. Millner, T. Miyata, E. Parmigiani, K. Schilling, G. Sekerková, R. V. Sillitoe, C. Sotelo, N. Uesaka, A. Wefers, R. J. T. Wingate and R. Hawkes, *Cerebellum*, 2015, 1–40.
2 J. D. Corrales, *Development*, 2004, **131**, 5581–5590.
3 R. R. Llinas, K. D. Walton and E. J. Lang, in *The Synaptic Organization of the Brain*, ed. G. M. Shepherd, Oxford University Press, New York, 2004, pp. 339–394.
4 A. Sudarov and A. L. Joyner, *Neural Dev.*, 2007, **2**, 26.
5 J. D. Corrales, S. Blaess, E. M. Mahoney and A. L. Joyner, *Development*, 2006, **133**, 1811–1821.
6 E. Legue, E. Riedel and A. L. Joyner, *Development*, 2015, **142**, 1661–1671.
7 S. Martinez, A. Andreu, N. Mecklenburg and D. Echevarria, *Front. Neuroanat.*, 2013, **7**, 18.
8 S. Patel and A. J. Barkovich, *Am. J. Neuroradiol.*, 2002, **23**, 1074–1087.
9 A. Goriely and M. BenAmar, *Phys. Rev. Lett.*, 2005, **94**, 198103.
10 M. BenAmar and A. Goriely, *J. Mech. Phys. Solids*, 2006, **53**, 2284–2319.
11 T. Tallinen, J. S. Biggins and L. Mahadevan, *Phys. Rev. Lett.*, 2013, **110**, 024302.
12 D. P. Richman, R. M. Stewart, J. W. Hutchinson and V. S. Caviness, *Science*, 1975, **189**, 18–21.
13 A. Goriely, M. G. D. Geers, G. A. Holzapfel, J. Jayamohan, A. Jérusalem, S. Sivaloganathan, W. Squier, J. A. W. van Dommelen, S. Waters and E. Kuhl, *Biomech. Model. Mechanobiol.*, 2015, 931–965.
14 T. Tallinen, J. Y. Chung, F. Rousseau, N. Girard, J. Lefevre and L. Mahadevan, *Nat. Phys.*, 2016, DOI: 10.1038/nphys3632.
15 E. Kuhl, *Nat. Phys.*, 2016, DOI: 10.1038/nphys3641.
16 H. G. Allen, *Analysis and Design of Structural Sandwich Panels*, Pergamon Press, Oxford, 1969.
17 M. A. Biot, *J. Appl. Math. Mech.*, 1937, **22**, 984–988.
18 B. Li, Y.-P. Cao, X.-Q. Feng and H. Gao, *Soft Matter*, 2012, **8**, 5728.
19 J. W. Hutchinson, *Philos. Trans. R. Soc., A*, 2014, **371**, 20120422.
20 H. Mei, R. Huang, J. Y. Chung, C. M. Stafford and H. H. Yu, *Appl. Phys. Lett.*, 2007, **90**, 151902.
21 P. Ciarletta, V. Balbi and E. Kuhl, *Phys. Rev. Lett.*, 2014, **113**, 248101.
22 L. Jin, A. Takei and J. W. Hutchinson, *J. Mech. Phys. Solids*, 2015, **81**, 22–40.
23 S. Budday, R. Nay, R. de Rooij, P. Steinmann, T. Wyrobek, T. C. Ovaert and E. Kuhl, *J. Mech. Behav. Biomed. Mater.*, 2015, **46**, 318–330.
24 E. Hohlfeld and L. Mahadevan, *Phys. Rev. Lett.*, 2011, **106**, 105702.
25 S. Budday, E. Kuhl and J. W. Hutchinson, *Philos. Mag.*, 2015, **95**, 3208–3224.
26 E. Lejeune, A. Javili and C. Linder, *Soft Matter*, 2016, **12**, 806–816.
27 J. Dervaux and M. BenAmar, *Phys. Rev. Lett.*, 2008, **101**, 068101.
28 E. Lejeune, A. Javili and C. Linder, *Extreme Mech. Lett.*, 2016, **7**, 10–17.
29 Z. Wu, J. Meng, Y. Liu, H. Li and R. Huang, *J. Appl. Mech.*, 2014, **81**, 081003.
30 Y. Cao and J. W. Hutchinson, *Proc. R. Soc. A*, 2012, **468**, 94–115.
31 F. Weiss, S. Cai, Y. Hu, M. Kang and R. Huang, *J. Appl. Phys.*, 2013, **114**, 073507.
32 S. Budday, P. Steinmann and E. Kuhl, *J. Mech. Phys. Solids*, 2014, **72**, 75–92.
33 A. Menzel and E. Kuhl, *Mech. Res. Commun.*, 2012, **42**, 1–14.
34 A. Javili, B. Dortdivanlioglu, E. Kuhl and C. Linder, *Comput. Mech.*, 2015, **56**, 405–420.
35 E. Rodriguez, A. Hoger and A. McCulloch, *J. Biomech.*, 1994, **27**, 455–467.
36 S. Göktepe, O. J. Abilez and E. Kuhl, *J. Mech. Phys. Solids*, 2010, **58**, 1661–1680.
37 C. Linder, M. Tkachuk and C. Miehe, *J. Mech. Phys. Solids*, 2011, **59**, 2134–2156.

38 M. Tkachuk and C. Linder, *Philos. Mag.*, 2012, **92**, 2779–2808.
39 A. Raina and C. Linder, *J. Mech. Phys. Solids*, 2014, **65**, 12–34.
40 Y. P. Cao, B. Li and X. Q. Feng, *Soft Matter*, 2012, **8**, 556–562.
41 X. Chen and J. Yin, *Soft Matter*, 2010, **6**, 5667–5680.
42 L. Jiang, C. Yang, L. Zhao and Q. Zheng, *Soft Matter*, 2014, **10**, 4603.
43 X. Zeng and S. Li, *Soft Matter*, 2012, **8**, 5765.
44 F. Sultan, *Nature*, 2002, **415**, 133–134.
45 K. E. Yopak, T. J. Lisney, R. B. Darlington, S. P. Collin, J. C. Montgomery and B. L. Finlay, *Proc. Natl. Acad. Sci. U. S. A.*, 2010, **107**, 12946–12951.
46 V. Mares and Z. Lodin, *Brain Res.*, 1970, **23**, 343–352.
47 M. L. Doughty, N. Delhaye-Bouchaud and J. Mariani, *J. Comp. Neurol.*, 1998, **399**, 306–320.
48 S. Budday, P. Steinmann, A. Goriely and E. Kuhl, *Extreme Mech. Lett.*, 2015, **4**, 193–198.
49 M. J. Razavi, T. Zhang, T. Liu and X. Wang, *Sci. Rep.*, 2015, **5**, 14477.
50 S. Cai, D. Chen, Z. Suo and R. C. Hayward, *Soft Matter*, 2012, **8**, 1301.
51 T. Tallinen, J. Y. Chung, J. S. Biggins and L. Mahadevan, *Proc. Natl. Acad. Sci. U. S. A.*, 2014, **111**, 12667.
52 Z. Wu, N. Bouklas and R. Huang, *Int. J. Solids Struct.*, 2012, **50**, 578–587.
53 M. A. Holland, K. E. Miller and E. Kuhl, *Ann. Biomed. Eng.*, 2015, **43**, 1640–1653.
54 O. V. Manyuhina, D. Mayett and J. M. Schwarz, *New J. Phys.*, 2014, **16**, 123058.